We are IntechOpen, the world's leading publisher of Open Access books Built by scientists, for scientists

4,800
Open access books available

122,000
International authors and editors

135M
Downloads

Our authors are among the

154
Countries delivered to

TOP 1%
most cited scientists

12.2%
Contributors from top 500 universities

WEB OF SCIENCE™

Selection of our books indexed in the Book Citation Index in Web of Science™ Core Collection (BKCI)

Interested in publishing with us?
Contact book.department@intechopen.com

Numbers displayed above are based on latest data collected.
For more information visit www.intechopen.com

Chapter 9

Microfluidic Sensors and Circuits for Internet of Things Applications

John Yan

Additional information is available at the end of the chapter

http://dx.doi.org/10.5772/64346

Abstract

As we move into the Internet of Things (IoT) and cloud computing era, the number of sensors deployed which seamlessly integrate themselves into environment is growing rapidly. These sensors should be minimally intrusive, both optically and mechanically, while providing high temporal and spatial contextual awareness of its environment. In this chapter, microfluidic sensors and circuits are presented to better bridge the physical and digital world for healthcare applications. Specifically, a discussion of cardiovascular sensing, glaucoma diagnosis and flexible tactile sensor arrays for smart skin application is presented.

Keywords: Circuits, digital health, internet of things, microfluidics, pervasive computing, sensors

1. Introduction

As we move into the Internet of Things (IoT) and cloud computing era, the number of sensors deployed that seamlessly integrate themselves into environment is growing rapidly [1–3]. The research and development challenges to create a smart and interconnected world necessitate a new paradigm in Internet architecture. This architecture requires the consideration of security, software platforms, ethical implications, standardization, smart sensors, and pragmatic business models. This chapter has honed down this broad vision to specifically focus on a few contributions from microfluidic sensors and circuits to better bridge the physical and digital world for healthcare applications.

1.1. Overview of Internet of Things for healthcare

As we move into the IoT and cloud computing era, the number of sensors deployed that seamlessly integrate themselves into environment is growing rapidly. This concept is descri-

bed a totally interconnected world where devices of every shape and size are manufactured with "smart" capabilities that allow them to communicate and interact with other devices, exchange data, make autonomous decisions, and perform useful tasks based on preset conditions. Figure 1 shows an ecosystem of IoT's relationship with people and the home within the modern cloud computing environment. Wearable devices and sensors would be ubiquitously employed to continuously monitor health and infrastructure that would subsequently be uploaded to data centers and archived as datasets. These datasets then provide the training necessary for data scientists and physicians to make intelligent predictions based on the behavior of its clients.

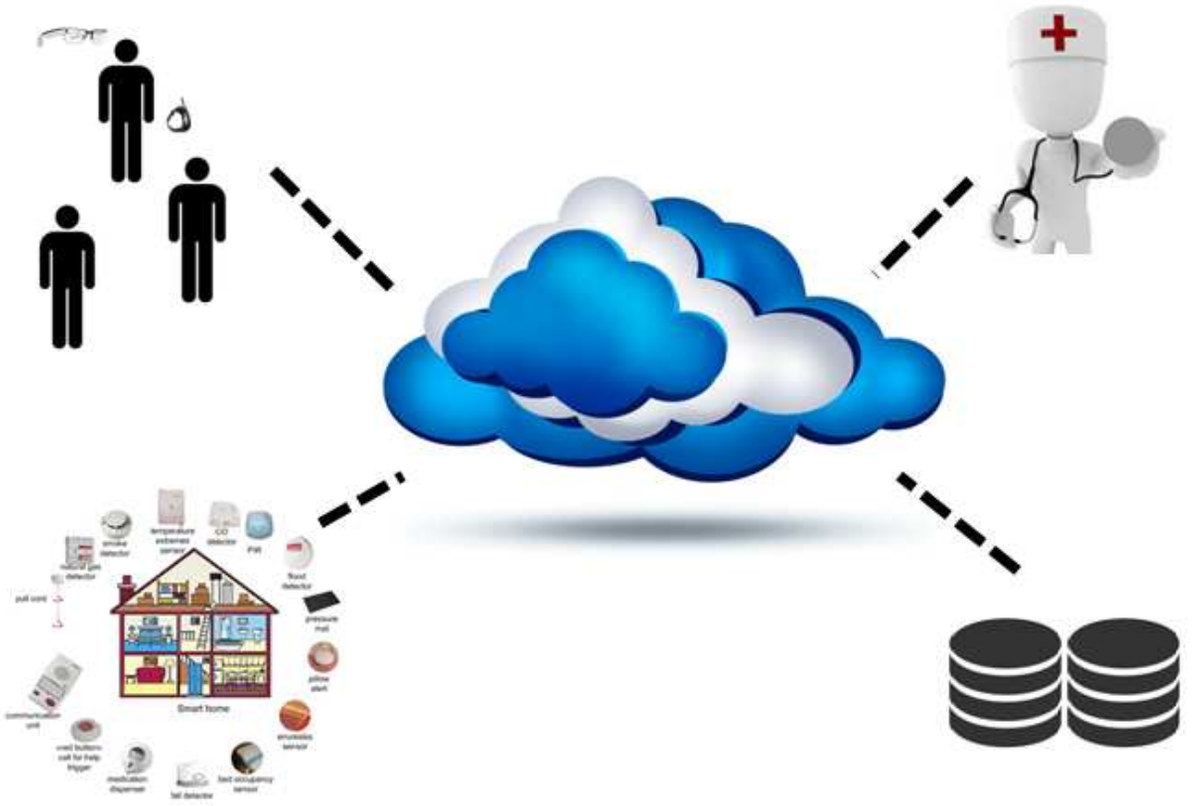

Figure 1. Data flow of Internet of Things devices for healthcare applications.

1.2. Microfluidics for IoT

Microfluidics is a multidisciplinary field intersecting engineering, nanotechnology, physics, and chemistry with practical applications to design systems in which small volumes of fluids will be handled [4–6]. In this chapter, we touch on the various facets of this multidisciplinary field and present applications on how microfluidic circuits and sensors can be utilized in an IoT environment. Figure 2 shows the variety of sensors and circuits for IoT healthcare applications ranging from cardiovascular sensing (to be integrated with smart-watch applications [7]) to unpowered microfluidic pressure sensors for glaucoma diagnosis [8] to flexible

http://dx.doi.org/10.5772/64346

tactile sensor arrays for smart skin applications [9]. Each of these devices will be addressed in more detail throughout this chapter.

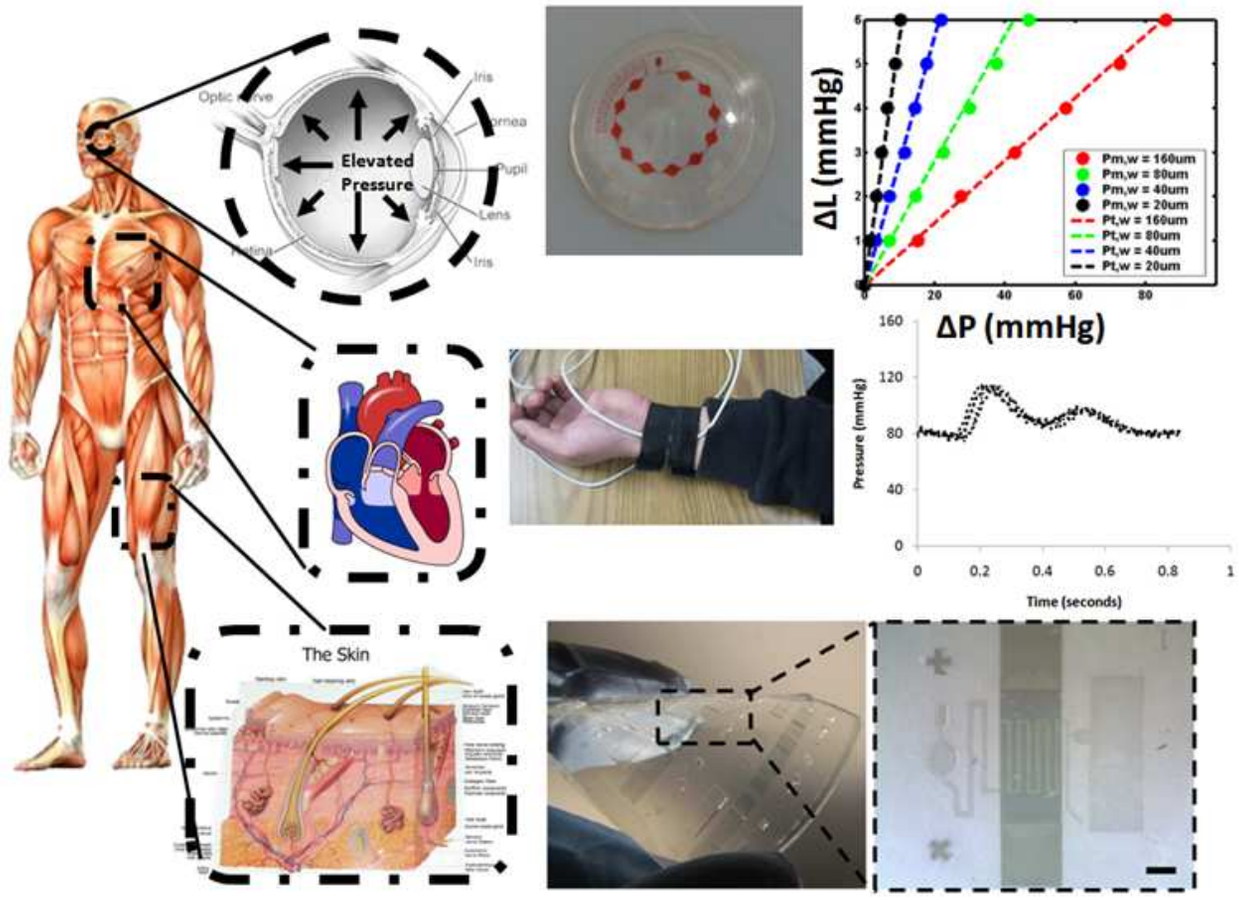

Figure 2. Example of IoT sensors for healthcare applications.

2. Coupled optomechanical pressure and flow measurements

Cardiovascular disease (CVD) is estimated to affect 81 million Americans adults [10]. An important determinant of these diseases is the arterial wall stiffness [11]. This section describes the development of a simple, non-invasive, real-time detection system that utilizes pulse wave velocity and pressure pulsation measurements to estimate vascular resistance and compliance in the radial artery that can provide the physician important diagnostic information. This system is realized by utilizing a 780 nm laser Doppler velocimeter to obtain the local flow rates and a piezoelectric pressure sensor to measure the pressure pulsation at the radial artery. Here, the sensor measurement results at the proximal and distal radial arteries are presented in both the time and frequency domain. While the presented results are demonstrated utilizing table-top instrument, ultimately this system can be completely integrated for a light-weight,

portable, real-time monitoring system that can potentially be embedded into textiles for seamless monitoring of important cardiovascular signals.

Figure 3 shows an overview of the IoT device that is used to monitor the vascular impedance through coupled optomechanical pressure (P) and flow (Q) measurements whose form factor should be small enough to be integrated with a wrist watch. On top of the biomaterial (bone, skin, blood, etc.) lies an optically transparent pressure sensor with integrated optics and electronics for digital signal processing and wireless communication to the cloud. Such a device facilitates the monitoring of signatures of cardiovascular disease using personalized datasets for real-time, continuous monitoring.

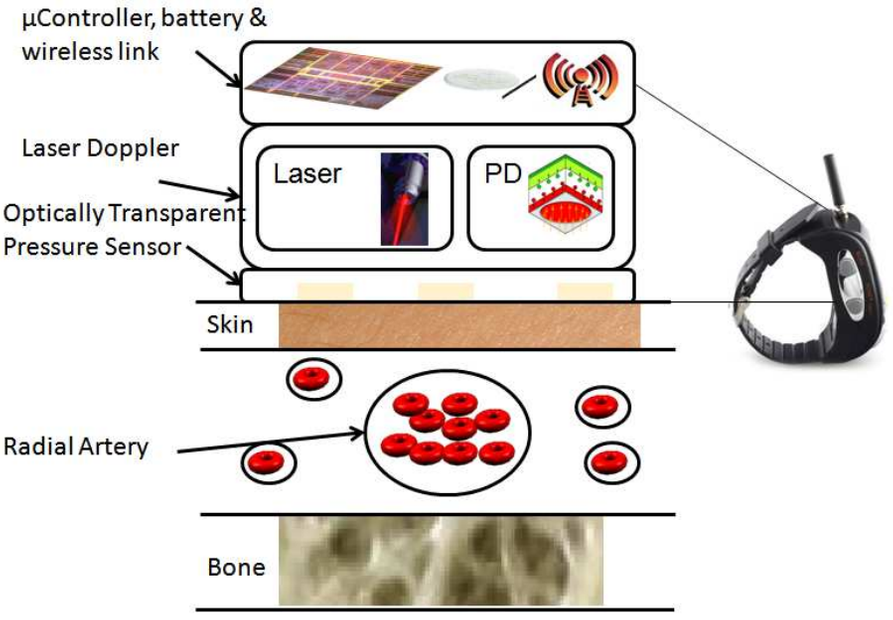

Figure 3. IoT vascular impedance assessment through coupled optomechanical pressure and flow measurements.

To measure the arterial flow, the laser Doppler principle, consisting of a laser light source shone on the radial artery and collection of the backscattered light collected by the photodiode, can be used. The total backscattered light consists of a component from the static tissue and a component with frequency shifted light, whose shifted amount is dependent on the speed of moving blood. These two components are collected and mixed on a photodetector whose corresponding photocurrent can then be post processed to indicate the velocity of moving red blood cells. This optical detection system should utilize $\lambda_0 = 780$ nm light with a typical output power of less than 1 mW of power. Therefore, the flow is:

$$Q = v_{s,r}\pi r^2 = -\frac{\Delta f}{n_{\text{bio,tissue}}}\lambda_0 \pi r^2 \tag{1}$$

where $n_{\text{bio,tissue}}(780\text{ nm}) \sim 2.6$.

http://dx.doi.org/10.5772/64346

The pressure sensor utilizes the concept tonometry to apply tension to the radial artery. The pressure sensor should be sufficiently flexible to conform to the skin and be optically transparent to the laser Doppler velocimeter system. Furthermore, it should have a sensitivity of 2 mmHg with a dynamic pressure range of 200 mmHg and an electromechanical bandwidth of 10 Hz. A detailed description of the construction and operation of such a pressure sensor built on microfluidic concepts will be described later on in this chapter.

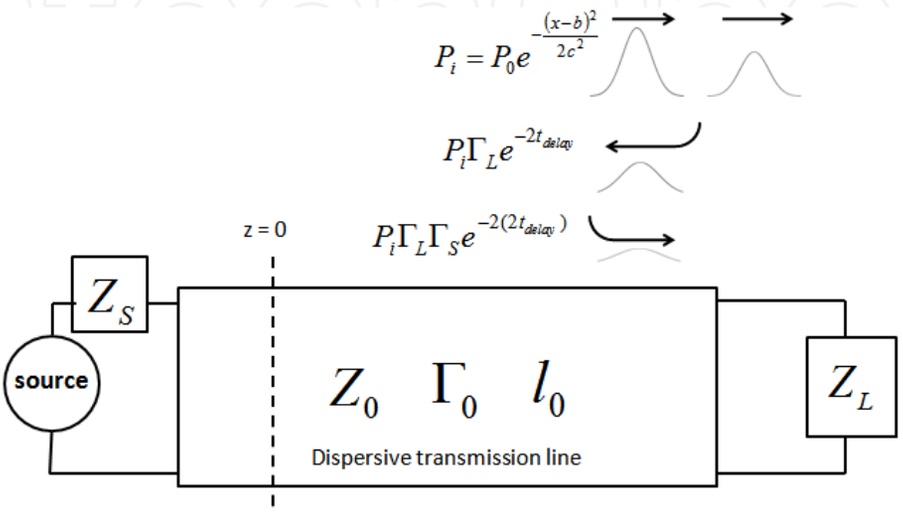

Figure 4. Model of cardiovascular system.

To describe the cardiovascular system, one can use transmission line analog between hydraulic transmission system of compliant tubes and an electrical transmission lines as shown Figure 4. Here, the blood flow and pressure waveforms are used to provide a baseline model to validate our measurement results where the signal source represents the heart. Based on the coupled Navier-Stokes equations [12]:

$$-\frac{\partial P}{\partial x} = QR + L\frac{\partial Q}{\partial t} \tag{2}$$

$$-\frac{\partial Q}{\partial x} = PG + C\frac{\partial P}{\partial t} \tag{3}$$

where arterial flow can be modeled as a dispersive transmission lines that broadens and distortions as it travels downward the hydraulic line. The different frequency components of propagation are then described by the standard impedance (Z_0) and reflection (Γ) relationships:

$$Z_0 = \sqrt{\frac{R + j\omega L}{G + j\omega C}} \tag{4}$$

$$\Gamma_L = \frac{Z_L - Z_0}{Z_L + Z_0} \tag{5}$$

$$\Gamma_S = \frac{Z_S - Z_0}{Z_S + Z_0} \tag{6}$$

where Γ_L is the reflection coefficient at the load and Γ_S is the reflection coefficient at the source. The mechanical resistance (R), compliance (C), and inductance (L) are governed by the following equations:

$$R = \frac{P}{Q} \tag{7}$$

$$C = \frac{\partial V}{\partial P} \tag{8}$$

$$L = \frac{P}{dQ/dt} \tag{9}$$

where resistance is the ratio of pressure over flow, compliance is the change of volume of fluid (∂P) over the change of pressure (∂P) and the inductance is pressure over the change of flow with respect to time (dQ/dt).

When the pressure and flow can be modeled as a Gaussian pulse with reflected waves that occur during discontinuities of impedances:

$$P(z=0) = P_i + P_r = P_i(1 + \Gamma e^{-2t_{\text{delay}}} + \Gamma^2 e^{-2(2t_{\text{delay}})} \cdots) \tag{10}$$

$$t_{\text{delay}} = \frac{1}{\text{length}} \frac{\omega}{\beta} \tag{11}$$

A sample of the measured results is shown in Figure 5 where the vascular impedance values of compliance, inductance and resistance can be obtained. Using reflection amplitudes, we can obtain the source and load impedance values. From the waveform, we not only know the vascular impedance at the point of optomechanical measurement but we can also estimate the vascular impedance at the source and load. The discontinuities along the arterial hydraulic line are a result of bifurcations that leads to reflected waves along the dispersive line. Time

http://dx.doi.org/10.5772/64346

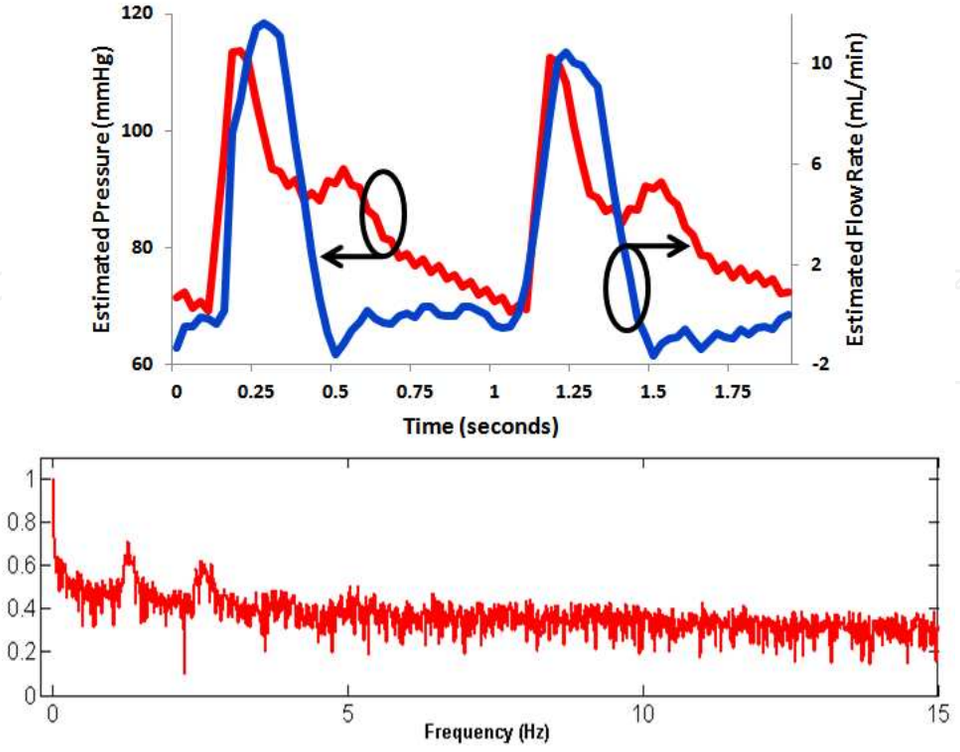

Figure 5. Sample of measured results from vascular impedance assessment of coupled optomechanical pressure and flow: (a) time domain; (b) frequency domain.

domain information can also be discrete Fourier transformed, whose signal can be improved with windowing functions due to the discrete sampling nature, to find spectral information.

3. Microfluidic sensor for point-of-care glaucoma diagnosis

An important microfluidic sensor developed for IoT applications is for the continuous monitoring of glaucoma that an estimated 67 million people are believed to suffer worldwide [13]. Patients with glaucoma are considered "well controlled" if their mean intraocular pressure (IOP) is lower than 21 mmHg. Owing to a rapidly aging population, it is estimated that the number of open angle glaucoma cases will increase to 3.4 million in 2020, making it the second leading cause of blindness and the first leading cause of irreversible blindness in the United States. Since unregulated IOP can lead to irreversible blindness by pinching the optic nerve, as seen in Figure 6, it is of paramount importance to monitor this pressure and make low-cost, point-of-care diagnostic tools available. Various wireless techniques have been conceived to continuously monitor intraocular pressure [16–19], which require radio frequency (RF) power transfer to power the device. However, a slew of potential health issues can arise from long term exposure to the high RF power transfer needed to power the device. Microfluidic solutions provides an unique solution due to its low-cost and biocompatible material construct that is additionally amendible to large-scale manufacturing.

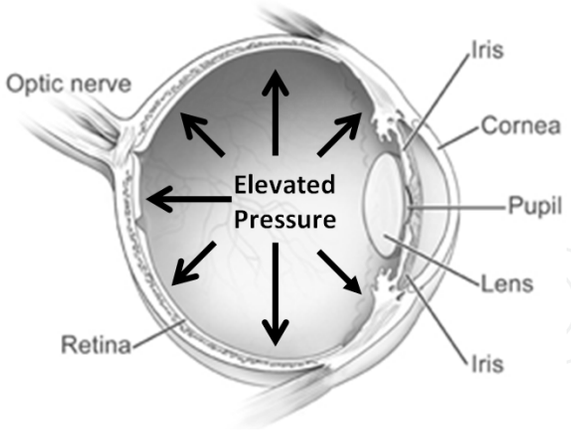

Figure 6. Glaucoma is a result of build up of intraocular pressure; figure adopted from [20].

The dynamical IOP measure is based on Laplace's principle where the pressure inside the hydraulic chamber (P_t) is dynamically determined by loading pressure and measured by the built-in microfluidic pressure sensor. The sensing membrane deflects and measures the pressure difference (P_s) at each contact point through the individual surface sensing element(s). Polydimethylsiloxane (PDMS) is used as the structural material to create the flexible, polymeric membrane and surface sensing for its elasticity and flexibility as well as excellent physical properties with a Young's modulus (E) of approximately 500 kPa [21].

The device to test the sensing principle is illustrated in Figure 7. It consists of a large, circular sensing chamber network with height H and radius r. This is followed by sensing channels of width w and height h, which act as the sensing elements. When local pressure is applied to the sensing chamber network, an internal strain is induced on the elastomer structure. This generates a pressure gradient internally within in the microfluidic network. As a result, the compression of the sensing chamber leds to an outward fluid displacement onto the sensing channel. As stress is released from the sensing chamber, the elastomer recovery properties of PDMS create a negative pressure to withdraw fluid from the sensing channel.

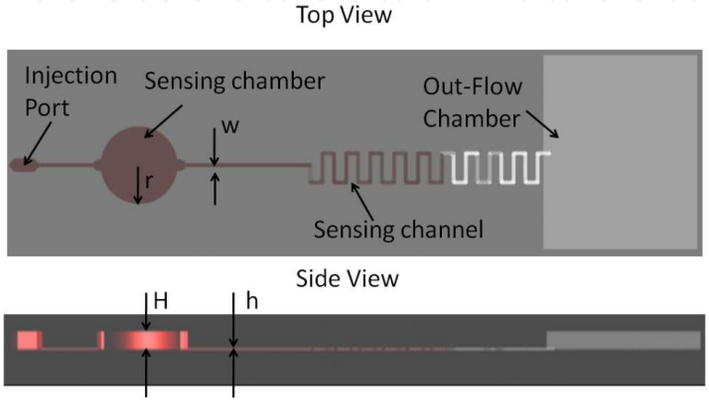

Figure 7. Schematic illustration of calibration device.

http://dx.doi.org/10.5772/64346

The microfluidic network is carefully designed to prevent air bubble formation at the sensing chamber during the injection process. This is done by installing an injection port before the sensing chamber network. Laplace valves at the entrance and exit of the sensing chamber are designed to prevent bubble cavitation as the fluid flows from the fluidic interconnects to the sensing chamber. To minimize compressive effects of displacement of air in the sensing channel during fluidic displacement, a large out-flow chamber is designed to have a volume a thousand times larger than the sensing channel, acting as a pressure relief conduit. A long, rectangular straight sensing channel is used to characterize the sensing principle of the device since its laminar flow profile characteristics are well understood. By optically observing the magnitude of fluidic displaced, the resulting pressure on the sensing chamber can be determined.

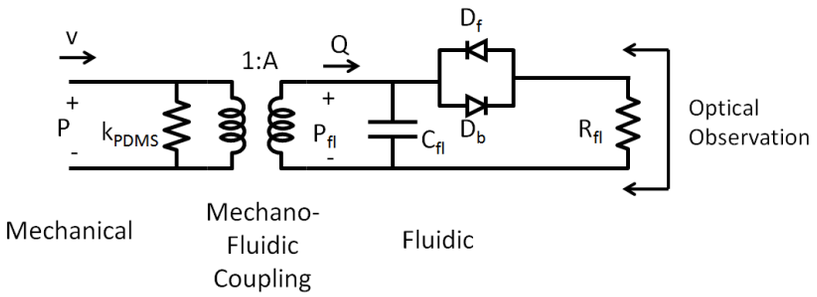

Figure 8. Equivalent circuit model of transducer.

The mechano-fluidic transduction can be modeled as a circuit network as shown in Figure 8. Pressure applied to the sensing chamber with a set velocity results in a corresponding flow of fluid due to the change in the internal pressure displacement. A transformer is used to model the conversion from solid mechanical displacement of the elastomer to the fluidic displacement in the microfluidic network. The displacement amplification A is set by the geometry of the sensing chamber and sensing channel. The stiffness of the sensing chamber is:

$$k_{\mathrm{PDMS}} = \frac{\mathrm{stress}}{\mathrm{strain}} \tag{12}$$

According to the strain-stress relationship, the change of the micro-chamber height can be expressed as, $\Delta H/H = \sigma/E$, where E is Young's Modulus of PDMS elastomer, and σ is the loading pressure. The displaced fluidic volume enters the incompressible microchannel, where the geometry (i.e., the cross-section area) determines the wetted length (Δl) of the colored fluid. Herein, the sensitivity (S) can be calculated as

$$S = \frac{P}{\Delta l} = \frac{whE}{\pi r^2 H} \tag{13}$$

To assess the frequency response of the sensor, the microfluidic sensing system can be modeled as a first-order linear circuit, in which the micro-chamber membrane compliance C and the microchannel resistance R are:

$$C = \frac{\pi r^2 H}{E} \tag{14}$$

$$R = \frac{12\mu\Delta l}{wh^3} \tag{15}$$

where μ is the viscosity of the sensing fluid. D_f and D_b represent the effect of surface tension and the resulting difference in internal pressure that needs to be overcome before the fluid can displace in the sensing channel. This surface tension is set by the surface properties of the material.

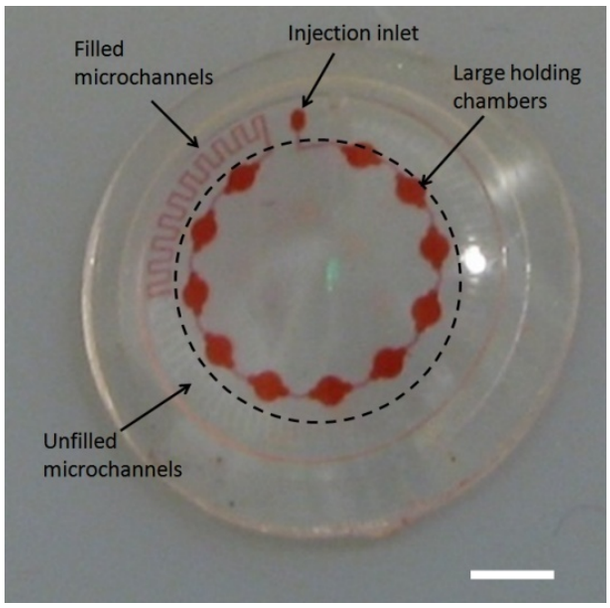

Figure 9. Optical photograph of the microfabricated device; scale bar is 5 mm.

To analyze the fluidic response, it is assumed that flow is dominated by pressure driven flow in the laminar region so the lubrication theory approximation can be used for the Navier-Stokes equation. The cutoff frequency, f_c, is set by the fluidic resistance and capacitance [22] as follows:

$$f_c = \frac{1}{2\pi\tau_{fl}} = \frac{1}{2\pi RC} = \frac{1}{2\pi\left(\frac{12\mu\Delta l}{wh^3}\right)\left(\frac{\pi r^2}{E}\Delta H\right)} \tag{16}$$

To accommodate the human cornea with an approximately a diameter of 7.8 mm, the microfluidic sensing chambers and corresponding meandered sensing channels are designed on the peripheral of the contact lens at the sclera area. A realized microfluidic device for IoT appli-

http://dx.doi.org/10.5772/64346

cations is shown in Figure 9. For the prototyped contact lens, the sensing channel length is over 80 mm with a sensing channel width of 20 μm. This corresponds to a dynamic range of 130 mmHg—more than sufficient for measuring the IOP. The characterization results of the device can be found in [8].

4. Microfluidic sensor for smart skin applications

Ubiquitous sensing and smart skin applications that leverage flexible substrates for ultra-high sensitivity pressure sensing is of great interest to the IoT community. This is especially of interest when the sensor optical properties can be tuned to be optically transparent for a host of applications. Figure 10 shows a 3 × 3 array of optical transparent, microfluidic pressure sensors.

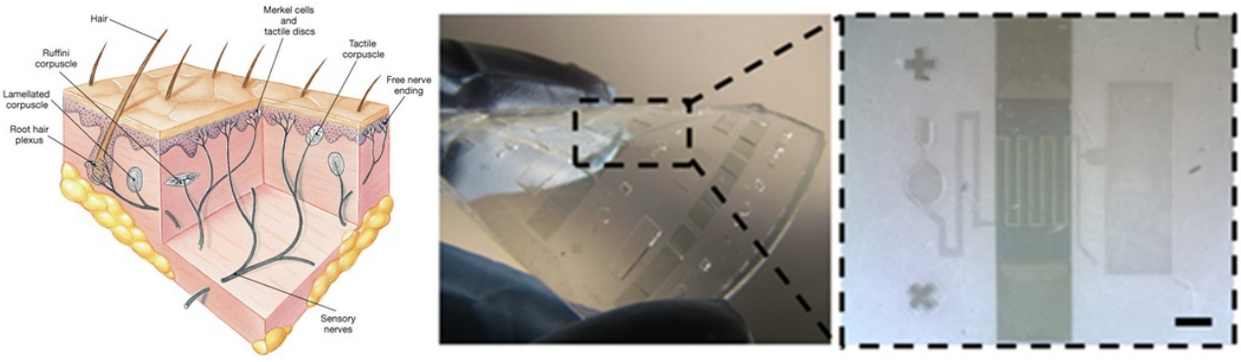

Figure 10. 3 × 3 array of optically transparent, microfluidic pressure sensor array (scale bar is 1 mm) for smart skin applications.

4.1. Device operation

The architecture of the microfluidic, capacitive pressure sensor is illustrated in Figure 11. It consists of a soft, micromachined elastomer to house fluid on a rigid plastic substrate. The highly deformable sensing chamber is designed to be tall and large to hold a volume of fluid much greater than the capacity of the sensing channel. Electrodes, in this case, transparent conductive oxide (TCO), are used to detect the degree of fluidic displacement as the sensing chamber deforms under applied pressures. Specifically, the large interfacial capacitance (>20 $\mu F/cm^2$) from the TCO and room temperature ionic liquid (RTIL) is employed [23]. To prevent air bubble generation, Laplace valves are placed at the exit and entrance of the sensing chambers. Optional mechanical concentrator(s) can be integrated to the sensor for additional sensitivity.

As pressure is applied at the sensing chamber, strain is induced on the elastomer housing the microfluidic network. In turn, an internal pressure gradient between the sensing chamber and sensing channel leads to an outward fluid displacement across the sensing channel. Due to the geometry difference between the sensing chamber and sensing channel, mechanical displace-

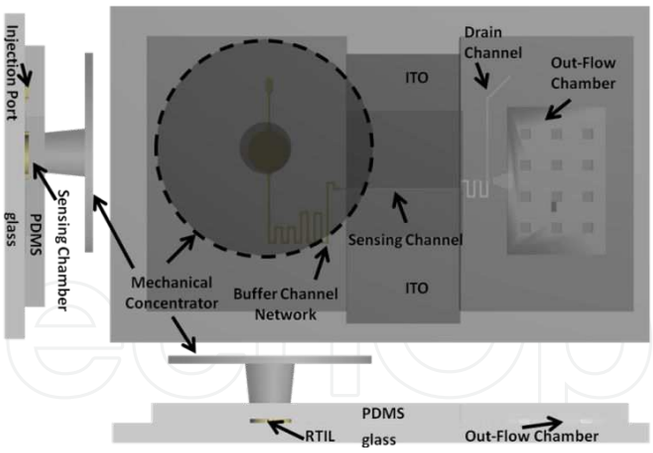

Figure 11. Microfluidic capacitive pressure sensor architecture.

ment amplification occurs as a result of the conservation of mass—a small compressive strain in the sensing chamber leads to a large displacement of fluidic across the sensing channel. Consequently, a change in the interfacial capacitance is detected across the coplanar electrodes. The causality of physics is illustrated in Figure 12, leading to a change in capacitance—where the strain on the elastomeric housing is exaggerated for illustrative purposes. When pressure is released from the sensing chamber, vacuum force is generated from the elastomer recovery, receding the fluid back to the sensing chamber and away from the coplanar electrodes. A mechanical concentrator, constructed out of rigid (~3 GPa) plastic, can subsequently be superimposed on top of the sensing chamber to further improve the sensitivity of the sensor. The concentrator serves to focus the mechanical pressure on the sensing chamber by using the area difference between the top disk area and the bottom disk that is in contact with the sensing chamber.

4.1.1. Interfacial capacitance

At the interface between RTIL and Indium Tin Oxide (ITO), there exists an electrochemical energy between Φ_m and π^* as shown in Figure 13a. In the inset, an example of an RTIL is shown. In this case 1-Butyl-3-Methylimidazolium Tetrafluroborate ($BMImBF_4$) has attractive properties of low surface tension and is readily available, consisting of an anion and a cation. In order to maintain electrostatic neutrality between the two materials, a thin layer of ions are collected at the surface. As a result, an interfacial capacitance is formed. The associated electrical circuit model is shown in Figure 13b. The equivalent circuit model of the interfacial capacitance, C_I, can be described by the Gouy-Chapman Model [24]:

$$\frac{1}{C_I} = \frac{1}{C_H} + \frac{1}{C_G} = \frac{2}{(w-g)l}\left(\frac{d_{OHP}}{\varepsilon_0\varepsilon_r} + \frac{L_D}{\varepsilon_0\varepsilon_r \cosh\left(\frac{z\Phi_0}{2U_t}\right)}\right) \cong \frac{2}{(w-g)l}\frac{d_{OHP}}{\varepsilon_0\varepsilon_r} \tag{17}$$

http://dx.doi.org/10.5772/64346

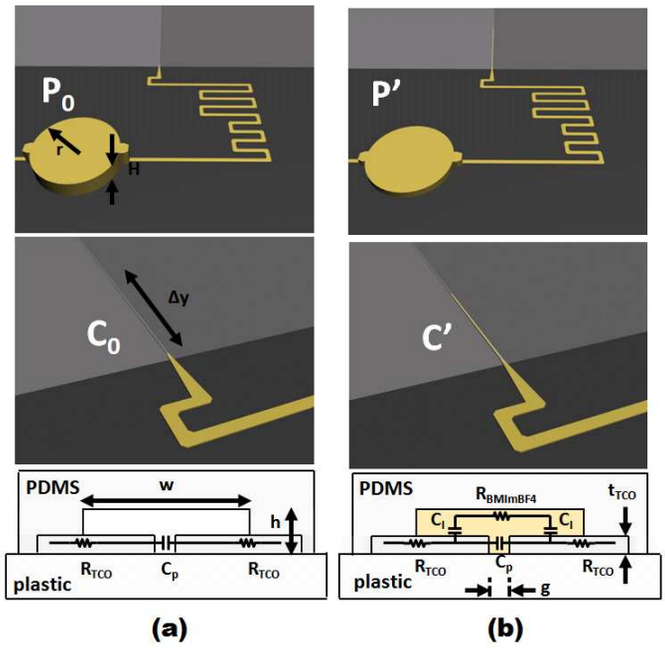

Figure 12. Illustration of device operation with equivalent circuit: (a) initial pressure and capacitance; (b) measured pressure and capacitance.

where w is the width of microfluidic channel, g is the gap between the electrodes, $\varepsilon_0\varepsilon_r/d_{OHP}$ is the capacitance per unit area, and l is the length of fluid overlap from the sensing channel mouth. The charge transfer resistance, R_{ct}, is a high-value resistance (~MΩ) due to tunnel current leakage can be described as

$$R_{ct} = \frac{RT}{nFi_0} \tag{18}$$

where R is the universal gas constant, T is the temperature, F is the Faraday constant, n is the number of electrons in the unit reaction and i_0 is the current. R_{oxide} and R_{bulk} are the finite resistance of the electrolyte and metal.

The associated change in fringe capacitance, C_p can be described as [25]

$$C_p = \varepsilon_0\varepsilon_{eff}\frac{K(k_0')}{K(k)} \tag{19}$$

where $K(k)$ is complete elliptic integrals of the first kind described as

$$k_0 = \frac{g}{s+g} \tag{20}$$

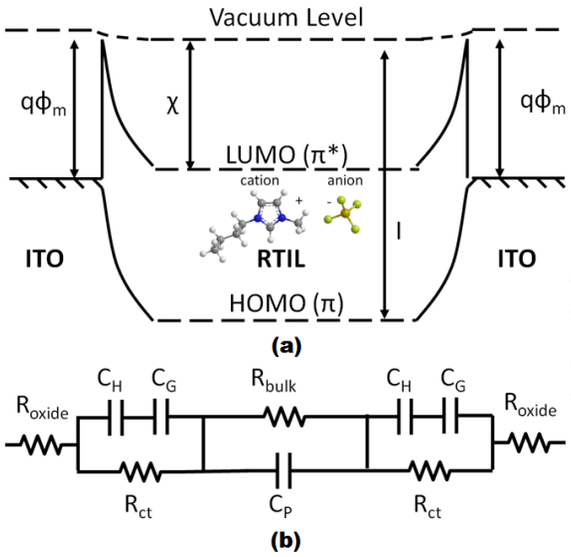

Figure 13. (a) Band diagram of the energy potential; (b) equivalent circuit model.

$$k_0^{'} = \sqrt{1 - k_0^2} \tag{21}$$

where g is the gap distance of the edge of the electrode from the symmetrical plane of the coplanar electrodes and s is the effective electrode distance as a result of the parasitic coplanar capacitance between the two electrodes whose value is typically much smaller than C_I.

4.1.2. Electromechanical model

The equivalent electromechanical circuit model is shown in Figure 14. According to the strain-stress relationship, the change of the micro-chamber height (H) can be expressed as, $\Delta H/H = \sigma/E$, where E is Young's Modulus of PDMS elastomer, and, σ is the loading pressure.

As normal pressure is applied at the sensing chamber, a resulting strain is induced on the elastomer housing the microfluidic network following the simple stress-strain relationship

$$\frac{\Delta P}{E} = \frac{\Delta H}{H} \tag{22}$$

As a result, an internal pressure gradient occurs between the sensing chamber and sensing channel in the microfluidic channel creating an outward fluid displacement across the sensing channel due to conversation of mass, as exhibited by the $\pi r^2 \Delta H = wh\,\Delta l$ relationship. By causalities in physics as previously described, a change in capacitance will be observed across the electrodes due to changes in pressure.

By inserting the stress-strain relationship and interfacial capacitance into the conversation of mass equation, the sensitivity of the device can be described by the following equation:

http://dx.doi.org/10.5772/64346

$$S = \frac{\partial C}{\partial P} = \frac{H}{E}\pi r^2 \frac{\varepsilon_0 \varepsilon_{\mathrm{r,fluid}}}{d_{\mathrm{double\,layer}}}\left(\frac{w-g}{2}\right)\frac{1}{wh}\frac{1}{2} \tag{23}$$

where H is the height of the sensing chamber, r is the radius of the sensing chamber, E is the Young's modulus of the membrane, w is the width of the sensing channel, g is the electrode gap, h is the height of the sensing channel and $\varepsilon_0\varepsilon_{\mathrm{r,fluid}}/d_{\mathrm{double\ layer}}$ is the interfacial capacitance per unit area. This equation shows that the sensitivity of the sensor can be easily tuned by adjusting the geometries of the microfluidic network.

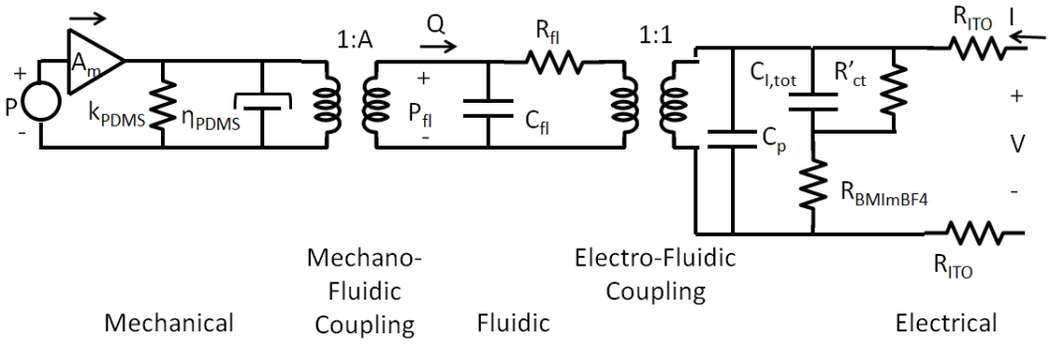

Figure 14. Equivalent electromechanical circuit model.

The fluidic resistance is assumed to operate by a pressure driven flow in the laminar region so the lubrication theory approximation can be used for the Navier-Stokes equation. The fluidic resistance, defined as ratio of hydrodynamic pressure over volume flow rate, of the sensing channel as

$$R = \frac{12\mu}{wh^3}\left[1 - \frac{h}{w}\left(\frac{192}{\pi^5}\sum_{n=1,3,5}^{\nabla}\frac{1}{n^5}\tanh\left(\frac{n\pi w}{2h}\right)\right)\right]^{-1} \approx \frac{12\mu\Delta L}{wh^3} \tag{24}$$

when $h << w$. The fluidic capacitance is described as the ratio of chamber volume over applied hydrodynamic pressure. For the sensing chamber, this can be modeled as

$$C = \frac{\pi r^2}{E}\Delta H \tag{25}$$

when $h << w$. The microfluidic resistance and capacitance are believed to play an important role in the frequency response of the sensor. The fluidic capacitance is described as the ratio of chamber volume over applied hydrodynamic pressure.

Additionally, the amplification of mechanical concentrator is simply:

$$A_{\mathrm{m}} = \left(\frac{D_{\mathrm{out}}}{D_{\mathrm{in}}} \right)^2 \tag{26}$$

where D_{out} is the upper diameter of the mechanical amplifier and D_{in} is the lower diameter of the mechanical amplifier [26].

4.2. Device fabrication

Techniques to fabricate microfluidics [27, 28] have been modified for these devices. A typical fabrication process is illustrated in Figure 15. The master mold, shown in Figure 16a, is fabricated by a two-step SU-8 process on a silicon substrate. The first step consists of forming the buffer channel, sensing channel, drain channel, and the associated microfluidic interconnects to a height of 15 μm. The second step consists of forming the sensing chamber, out-flow chambers and injection port to have a height of 200 μm. The thin film ITO electrodes are patterned with a hydrochloric acid wet etch process and traditional photolithography. Next, the PDMS elastomer is fabricated with a 10:1 (base: agent) mixture to create a thick replica mold of 1 mm. This replica mold is subsequently aligned to the ITO electrode pattern and bonded onto the glass substrate through oxygen plasma pretreatment as shown in Figure 16c.

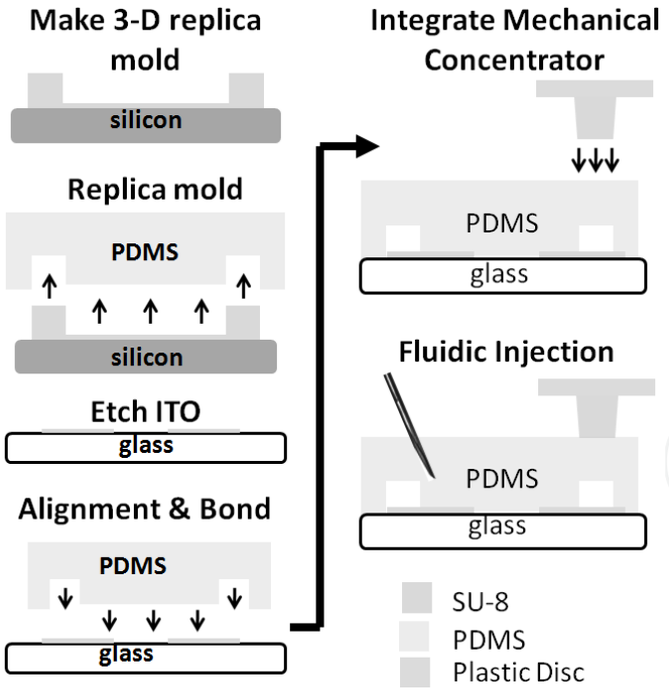

Figure 15. Microfabrication process.

A BD 30½ G needle is inserted into the injection port of the elastomer housing and a controlled volume of fluid is infused into the microfluidic network from a glass syringe using a syringe pump at a calibrated flow rate. Due to the small diameter of the gauge needle, the puncture

http://dx.doi.org/10.5772/64346

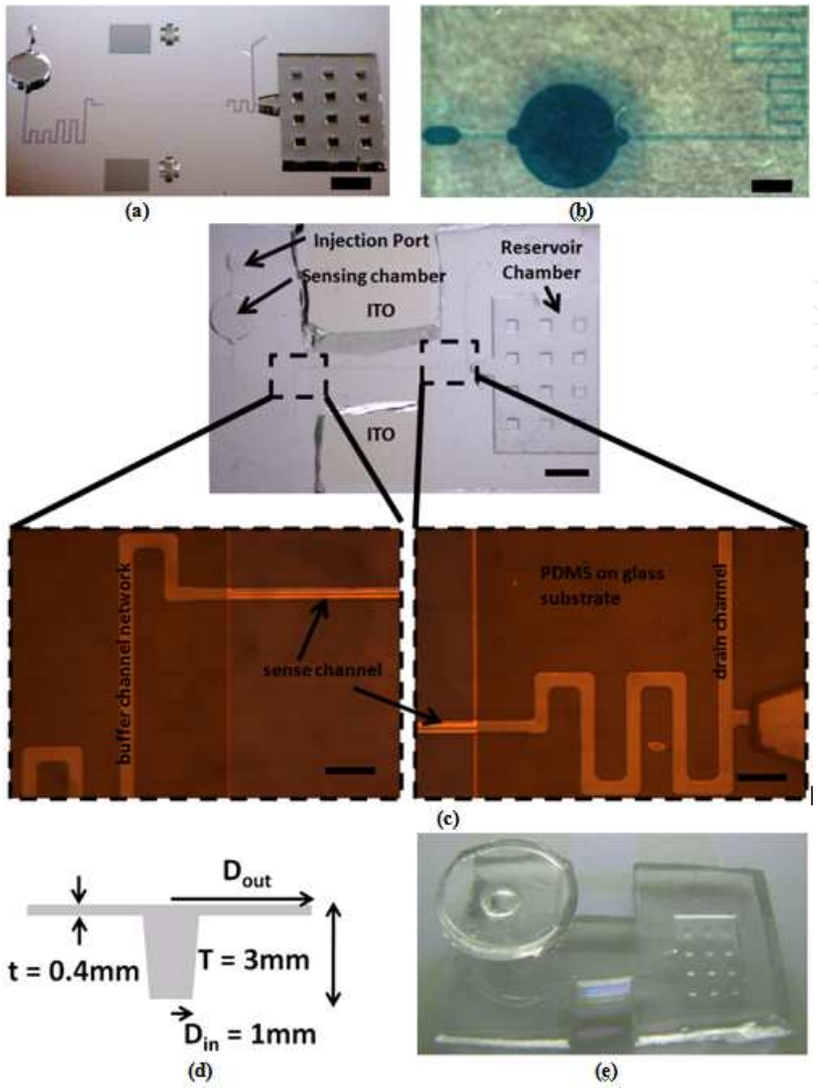

Figure 16. (a) 3-D replica mold. (b and c) Device. (d) Schematic of mechanical amplifier. (e) Mechanical amplifier integrated with microfluidic, capacitive pressure sensor.

hole is self-sealed after withdrawal due to the elastomeric properties of the PDMS. For illustrative purposes, dyed glycerol is injected as shown in Figure 16b. After the injection of RTIL, the patterned microchannels become invisible due to the close refractive index between $BMImBF_4$ (1.42) and the PDMS housing (1.4). The mechanical concentrator is constructed out of polystyrene, for its combination of mechanical rigidity (~3 GPa), optical transparency, low-cost and micromachinability with a programmable, CO_2 laser (universal laser systems), whose schematic is illustrated in Figure 16d. Furthermore, polystyrene and PDMS can form covalent bonding through oxygen plasma treatment leading to simple integration. This is a result of the plasma, creating hydrogen bondings of silanol groups with C-OH and COOH moieties on the oxidized-rich polystyrene surface [29]. Additionally, the PDMS molds can be transferred to a suite of other plastic substrates through simple plasma assisted bonding to form an array of flexible pressure sensors [30]. The finished device is illustrated in Figure 16e.

4.3. Characterization setup

The test setup to evaluate the sensor sensitivity is shown in Figure 17. It consists of a force gauge and a step motor mounted onto an optical table. As controlled normal pressure is applied to the sensing chamber, the fluidic displacement within the sensing channel is monitored with an optical microscope. The electrical impedance spectroscopy is monitored with a precision LCR meter and Labview software. The frequency dependent double layer capacitance response is plotted in Figure 18 where increments of 1 kPa are applied to the pressure sensor. The response double layer capacitance at the ITO/BMImBF$_4$ interface has a peak capacitance of approximately 25 μF/cm^2 at 30 Hz. This high capacitance per unit area indicates a successful surface engineering to roughen the electrode surface.

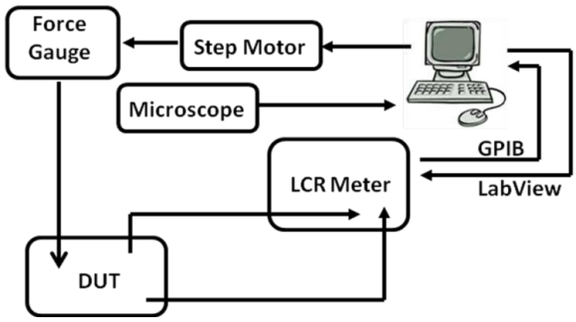

Figure 17. Measurement setup for sensitivity.

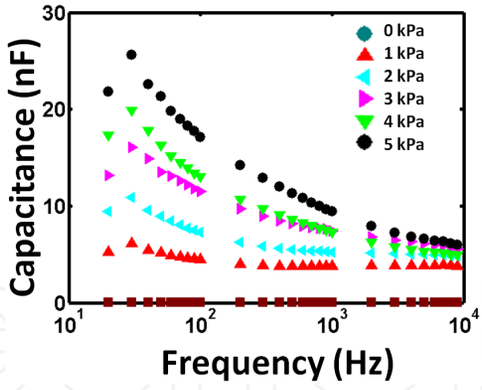

Figure 18. Frequency-dependent double layer capacitance versus frequency for applied pressure in increments of 1 kPa.

Images of the optically transparent, flexible pressure sensor array are shown in Figure 19 with device dimensions of w = 100 μm, g = 20 μm, h = 15 μm, r = 500 μm, H = 150 μm, t_{PDMS} = 500 μm, and t_{TCP} = 1.5 μm. A meandered fluidic sensing channel geometry with interdigitated sensing electrodes was chosen for a compact device with a larger dynamic range over the straight channel sensing channel topology. Linear capacitive pressure analog response is measured over the dynamic range of approximately 96 kPa. Beyond the dynamic range, the capacitive response saturates. The measured capacitance versus pressure sensitivity is

http://dx.doi.org/10.5772/64346

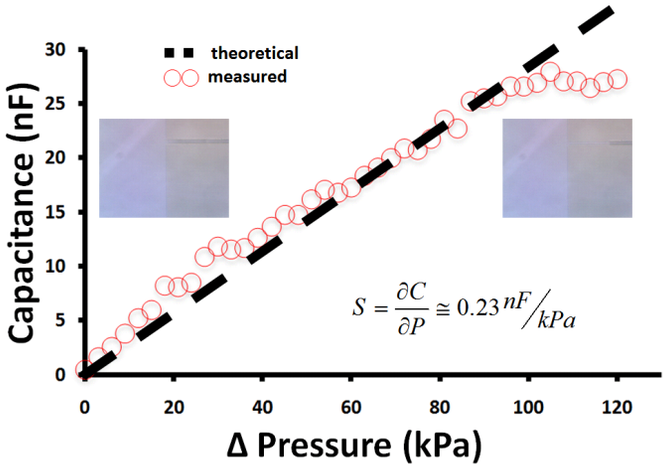

Figure 19. Measured capacitance versus applied pressure at 30 Hz of single pressure sensor within array (insets show images of fluidic displacement as a result of applied pressure with measured corresponding capacitance).

approximately 0.23 nF/kPa. The experimental sensitivity agrees well with the theoretically predicted sensitivity equation through carefully characterization of the interfacial capacitance and effective Young's modulus of the sensing chamber structure.

To further improve the sensitivity of the device, mechanical amplification is investigated. With the mechanical amplification (A_m), the new sensitivity (S') increases by the following expression:

$$S' = A_m S \tag{27}$$

where A_m is set by D_{out} and D_{in} of the mechanical amplifier as previous described in the electromechanical model. The mechanical concentrator is constructed out of polystyrene, for its combination of mechanical rigidity (~3 GPa), optical transparency, low-cost and micromachinability with a programmable CO_2 laser.

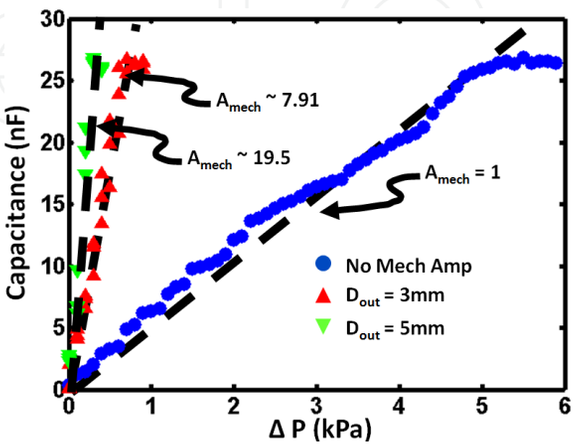

Figure 20. Measured capacitance versus pressure response at 30 Hz underlying the empirical computation model.

The measured capacitance versus pressure response are overlaid with theoretical sensitivity, at a fixed frequency of 30 Hz, is shown in Figure 20. The dynamic range of the device is set by the length of the sensing channel. Beyond the dynamic range, the capacitive response saturates, exhibited thorough measurement results. With the mechanical concentrators, a mechanical gain of approximately 19.5 is measured for D_{out} = 5 mm and D_{in} = 1 mm. A gain of 7.91 is measured when D_{out} = 3 mm. The disparity between the theoretical and measured mechanical concentrator amplification is believed to lie in the inability for the forces to sum across the surface of the applied pressure and focus onto the sensing chamber.

4.4. Time-resolved measurements

To shed light on the relaxation time constant of the pressure sensor, time-resolved measurements are conducted. A schematic of the test setup is shown in Figure 21. A 30 Hz sine wave with 500 mV_{pk-pk} is applied from a signal generator applied to one electrode and a ceramic capacitor with a value of 7.4 μF is connected to ground and parallel with the oscilloscope. The internal envelope detector function in the oscilloscope is used to smooth AC ripples. The data is saved on the oscilloscope and processed in Matlab®. The interface circuit does not amplify or compensate for the nonlinear characteristics of the sensor. The measured capacitance value follows the applied input pressure well indicating repeatability and negligible hysteresis.

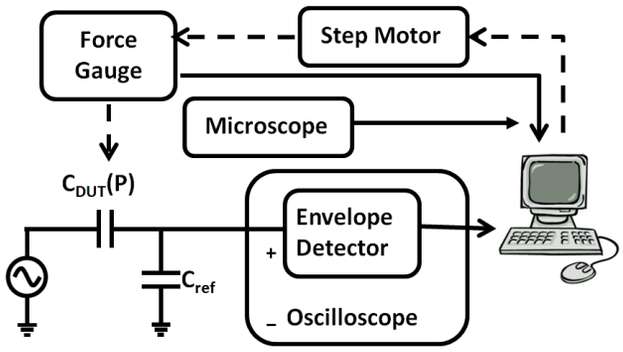

Figure 21. Time-resolved test setup.

A computer-controlled step motor and a force sensor are used to apply an external pressure of 1000 Pa and 500 Pa, respectively, at 1 Hz and 2 Hz, while measuring the electrical response. The fluid is displaced in the middle-length of the sensing channel with an offset pressure of approximately 2 kPa. The measured electrical response of the mechanical input is plotted in Figure 22, indicating repeatability and negligible hysteresis of the sensor. There is an observable phase lag (τ) between the applied input pressure and the measured voltage response. This is believed to be of three components: (1) elastomeric PDMS recovery response (τ_{PDMS}), (2) propagating velocity of the fluid (τ_{fl}), and (3) the steady-state charge buildup of the interfacial capacitance (τ_{RC}):

$$\tau = \tau_{PDMS} + \tau_{fl} + \tau_{RC} \tag{28}$$

http://dx.doi.org/10.5772/64346

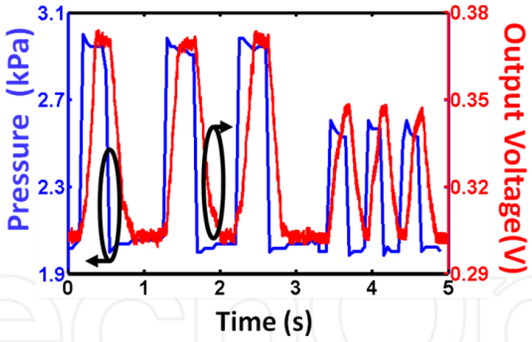

Figure 22. Time-resolved measurement results with applied input pressure on the left *y*-axis and corresponding output voltage on the right *y*-axis.

The frequency is not limited by the elastomer response, since PDMS has a frequency response in excess of 200 Hz [31]. The τ_{RC} is set by the electrical properties of the device that is on the order of μs. This also is not the limiting factor where R ranges from 30 to 100 Ω and C ranges from 0 to 27 nF. This arrives to the conclusion that the dominating factor that limits the frequency performance of the pressure sensor is the fluidic response set by the viscosity. To analyze the fluidic response, the flow is assumed to be dominated by a pressure driven flow in the laminar region. Thus, the lubrication theory approximation can be used for the Navier-Stokes equation. The resulting cutoff frequency, f_c, is then approximately set by the fluidic resistance and capacitance from the following equation:

$$f_c = \frac{1}{2\pi\tau_{fl}} = \frac{1}{2\pi RC} = \frac{1}{2\pi\left(\frac{12\mu\Delta L}{wh^3}\right)\left(\frac{\pi r^2}{E}\Delta H\right)} = \frac{E^3 w^2 h^4}{24\mu\pi^3 r^4 H^2 \Delta P^2} \tag{29}$$

where E is the effective Young's modulus of the sensing chamber w and h are the width and height of the sensing channel, μ is the viscosity of the fluid (approximately 233 cP at room temperature[32]), r and H are the radius and height of the sensing chamber and ΔP is the pressure change over a period. A response and relaxation time is observed to be dependent on the fluidic RC time constant. This shows that the response time of the sensor can easily be tuned by adjusting the width and height of the sensing channel or the geometries of the sensing chamber. This also shows that the effective Young's modulus of the fluidic encasing will improve the frequency response, which can be tuned by adjusting different ratios of PDMS [33]. Furthermore, the magnitude of the input pressure and velocity of mechanical input also affects frequency response. The overshoot in the measured pressure indicates the viscoelastic nature of the elastomer. The underdamped measured output voltage suggests an RC time constant response corresponding with the large interfacial capacitance.

4.5. Summary of microfluidic sensor for smart skin applications

The development of ultra-high sensitivity, capacitive pressure sensors using ionic liquids is presented. These ultra-high sensitivities are achieved through three levels of amplification: (i)

fluidic displacement amplification through the geometric volume difference between the large sensing chamber and small sensing channel; (ii) ultra-high, capacitance formed at the interface between the electrode-liquid surface; and (iii) mechanical concentration of the pressure onto the sensing chamber through the construction of a rigid construct relatively to the elastomeric housing. The measured results demonstrate a 2000× improvement sensitivity over traditional capacitive pressure sensors. Repeatability and hysteresis are investigated through time-resolved measurements demonstrating excellent performance. In addition to ultra-high sensitivity, the pressure sensor is constructed out of optically transparent material; here it displays a linear response and has a low-cost, simple fabrication process. Without the mechanical amplifier, this sensor can be readily integrated with other lab-on-chip components constructed out of PDMS. With the addition of the mechanical amplifier, such sensors have potential applications in ultra-high sensitivity tactile sensing.

Author details

John Yan*

Address all correspondence to: john.yan@mail.npu.edu

Northwestern Polytechnic University, Fremont, CA, USA

References

[1] J. Stankovic, "Research Directions for the Internet of Things," IEEE Internet Things J., vol. 1, no. 1, pp. 3–9, March 2014.

[2] C. Perera, A. Zaslavsky, C. Liu, M. Compton, P. Christen, Georgakopoulos, D., "Sensor search techniques for sensing as a service architecture for the Internet of Things," IEEE Sensors J., vol. 14, no. 2, pp. 406–420, April 2014.

[3] K. Lyytinen, Y. J. Yoo, "Issues and Challenges in Ubiquitous Computing," Communications of the ACM, vol. 45, no. 12, 62–65, 2002.

[4] G. M. Whitesides, "The Origins and the Future of Microfluidics," Nature 442, pp. 368–373, July 2006.

[5] N. T. Nguyen, S. T. Werely, Fundamentals and Applications of Microfluidics. Norwood, MA: Artech House, 2002.

[6] T. Thorsen, S. J. Maerkl, S. R. Quake, "Microfluidic Large-scale Integration," Science, vol. 298, no. 5593, pp. 580–584, October 2002.

[7] J. J. Yan, et al., "Vascular Impedance Assessment through Coupled Optomechanical Pressure and Flow Measurements," 11th Annual UC Systemwide Bioengineering Symposium, June 2010, Davis, CA.

[8] J. J. Yan, "An Unpowered, Wireless Contact Lens Pressure Sensor for Point-Of-Care Glaucoma Diagnosis," Proceedings of 33rd IEEE EMB Conference, pp. 2522–2525, August 30th–September 3rd 2011, Boston, MA.

[9] J. J. Yan, "Micromachined Optically Transparent, Flexible Pressure Sensor Array Exhibiting Ultra-High Sensitivity," J. Micro/Nanolithography, MEMS MOEMS, vol. 11, no. 1, pp. 013005-1–013005-5, February 2012.

[10] D. Lloyd-Jones, et al., "Heart disease and stroke statistics – 2010 update: a report from the American Heart Association," Circulation. Vol. 121, pp. e46–e215, 2010.

[11] F. Mattace-Raso, et. al., "Arterial stiffness and risk of coronary heart disease and stroke: The Rotterdam Study," Circulation vol. 113, pp. 657–663, 2006.

[12] B. R. Munson, D. F. Young, T. H. Okiishi – 1990 – New York Fundamentals of Fluid Mechanics.

[13] H. A. Quigley, A. T. Broman, "The Number of People with Glaucoma Worldwide in 2010 and 2020," Br. J. Ophthalmol., vol. 90, pp. 262–267, March 2006.

[14] J. M. Tielsch, et al., "A Population-Based Evaluation of Glaucoma Screening – The Baltimore Eye Survey," Am. J. Epidemiol., vol. 134, pp. 1102–1110, 15 November 1991.

[15] D. S. Friedman, et al., "Prevalence of Open-angle Glaucoma Among Adults in the United States," Arch. Ophthalmol., vol. 122, pp. 532–538, April 2004.

[16] K. C. Katuri, et al., "Intraocular Pressure Monitoring Sensors," IEEE Sensors J., vol. 8, pp. 12–19, January–February 2008.

[17] R. M. H. a. K. D. Wise, "An Intraocular Pressure Sensor Based On A glass Reflow Process," Workshop on Solid State Sensors and Actuators, Hilton Head, pp. 49–52, 6–10June 2010.

[18] M. Leonardi, et al., "First Steps Toward Noninvasive Intraocular Pressure Monitoring with a Sensing Contact Lens," Invest. Ophthalmol. Vis. Sci., vol. 45, pp. 3113–3117, September 2004.

[19] P. J. Chen, et al., "Unpowered Spiral-tube Parylene Pressure Sensor for Intraocular Pressure Sensing," Sensors Actuators A-Phys., vol. 127, pp. 276–282, 13 March 2006.

[20] Available: http://www.nei.nih.gov/health/glaucoma/.

[21] J. C. Lotters, et al., "The Mechanical Properties of the Rubber Elastic Polymer Polydimethylsiloxane for Sensor Applications," J. Micromech. Microeng., vol. 7, pp. 145–147, September 1997.

[22] D. Kim, et al., "A Method for Dynamic System Characterization using Hydraulic Series Resistance," Lab Chip, vol. 6, pp. 639–644, 2006.

[23] T. Torimoto, et al., "New Frontiers in Materials Science Opened by Ionic Liquids," Adv. Mater., vol. 22, pp. 1196–1221, 19 March 2010.

[24] A. J. Bard, L. R. Faulkner, Electrochemical Methods: Fundamentals and Applications, 2nd ed. New York: Wiley, 2001.

[25] H. A. Wheeler, "Transmission-Line Properties of Parallel Strips Separated by a Dielectric Sheet," IEEE Trans. Microwave Theory Tech., vol. MTT-13, no. 2, 178–185, 1965.

[26] Y.-M. L. I-Kuan Lin, Y. Liu, K.-S. Chen, X. Zhang, "Elastic and Viscoelastic Characterization of Polydimethylsiloxane (PDMS) for Cell-Mechanics Applications," Mater. Res. Soc. Symp. Proc., vol. 1052, 2008.

[27] S. R. Quake, A. Scherer, "From Micro- to Nanofabrication with Soft Materials," Science, vol. 290, pp. 1536–1540, 2000.

[28] J. C. McDonald, D. C. Duffy, J. R. Anderson, D. T. Chiu, H. K. Wu, O. J. A. Schueller, G. M. Whitesides, "Fabrication of Microfluidic Systems in Poly(dimethylsiloxane)," Electrophoresis, vol. 21, no. 1, pp. 27–40, 2000.

[29] A. Bubendorfer, et al., "Microfabrication of PDMS Microchannels using SU-8/PMMA Moldings and Their Sealing to Polystyrene Substrates," Smart Mater. Struct., vol. 16, pp. 367–371, April 2007.

[30] J. J. Yan, "Optically Transparent, Flexible Pressure Sensor Array Micromachined Utilizing Plasma Assisted Bonding," Proc. SPIE MOEMS-MEMS, vol. 8248, pp. 824803-1–824803-8, 21–26 January 2012, San Francisco, CA.

[31] M. A. Unger, et al., "Monolithic Microfabricated Valves and Pumps by Multilayer Soft Lithography," Science, vol. 288, pp. 113–116, 7 April 2000.

[32] P. G. Heiden, "Ionic Liquids in Chemical Analysis," Choice: Curr. Rev. Acad. Librar., vol. 47, pp. 712–712, 2009.

[33] K. Khanafer, et al., "Effects of Strain Rate, Mixing Ratio, and Stress-Strain Definition on the Mechanical Behavior of the Polydimethylsiloxane (PDMS) Material as Related to its Biological Applications," Biomed. Microdevices, vol. 11, pp. 503–508, April 2009.